Computers and Fluids 208 (2020) 104625

Contents lists available at ScienceDirect

Computers and Fluids

journal homepage: www.elsevier.com/locate/compfluid

A new 6th-order WENO scheme with modified stencils

Yahui Wang [a,b], Yulong Du [c], Kunlei Zhao [a,b], Li Yuan [a,b,*]

[a] ICMSEC and LSEC, Academy of Mathematics and Systems Science, Chinese Academy of Sciences, Beijing, 100190, PR China
[b] School of Mathematical Sciences, University of Chinese Academy of Sciences, Beijing, 100190, PR China
[c] School of Mathematics and Systems Science, Beihang University, Beijing, 100191, PR China

ARTICLE INFO

Article history:
Received 10 October 2019
Revised 9 March 2020
Accepted 8 June 2020
Available online 13 June 2020

Keywords:
WENO scheme
Sixth-order accuracy
Modified stencil
Hyperbolic conservation law

ABSTRACT

In this article, a new 6th-order weighted essentially non-oscillatory (WENO) scheme is developed. As with previous 6th-order central-upwind WENO schemes, the present scheme is a convex combination of four candidate linear reconstructions. The difference is that the most upwind and downwind stencils use four cell values, while the inner two stencils nominally use three cell values but the original quadratic reconstructions are modified to be 4th-order approximations by adding cubic correction terms involving the five cell values of the classical 5th-order WENO scheme. Sixth-order accuracy of the new scheme in smooth regions including critical points is achieved by using a reference smoothness indicator. Several numerical examples show that the new scheme has higher resolution compared with the recently developed 6th-order WENO schemes.

1. Introduction

The detailed simulation of complex shock waves and fine scale structures in compressible flows requires robust shock capturing methods with small dissipation and dispersion errors. High-order numerical methods for hyperbolic conservation laws provide an effective means for the simulation of complex compressible flows. Many high-order high-resolution methods have been developed in the past four decades, such as piecewise parabolic method (PPM) [1], essentially non-oscillatory schemes (ENO) [2,3], weighted ENO schemes (WENO) [4,5], discontinuous Galerkin methods [6,7], monotonicity-preserving schemes [8], and so on. These methods have been shown to be capable of producing satisfactory numerical results, and there have been a lot of subsequent studies on them for improving computational efficiency, robustness, accuracy, and reducing dissipation and dispersion errors.

The classical 5th-order WENO scheme [5] has attracted a great deal of attention due to the merit of easy implementation, high order accuracy in smooth regions, and essentially non-oscillatory property near discontinuities. However, the scheme is a bit dissipative for the simulation of small scale structures in smooth regions. Up to now, four different approaches have been developed for reducing numerical dissipation of the classical WENO scheme. The first approach, e.g., [9–11], is to hybridize a low-dissipation scheme which is dominant in smooth regions and a WENO scheme which is dominant in non-smooth regions. The second approach, e.g., [12,13], is to modify the weights to cure accuracy degeneration at critical points and distribute a little more weights to the less smooth stencils. There are multiple strategies for this approach, e.g., a mapping function (WENO-M [12]), a global reference smoothness indicator (WENO-Z [13,14]), and smoothness indicators based on L_1-norm (WENO-P [15]). The third approach is to modify the stencils and corresponding weights, like P-WENO [16], WENO-ZQ [17] and WENO-MS [18] schemes. The above three approaches use three candidate stencils over the same five-point global stencil as the classical 5th-order WENO scheme. The fourth approach is to add an additional downwind candidate stencil to the classical 5th-order upwind WENO scheme. This approach started from the 6-point WENO-SYMOO and WENO-SYMBO schemes in [19], which are designed based on the idea of optimal order of accuracy and optimal bandwidth-resolving efficiency, respectively. However, the order of the WENO-SYMBO scheme degenerates even in smooth regions, and the order-optimized WENO-SYMOO scheme is unstable near contact discontinuities even when only moderate discontinuities are involved. Ref. [20] defined a smoothness indicator for the downwind stencil and devised a reference smoothness indicator τ similar to that in the WENO-Z scheme [13] for achieving the optimal order of accuracy. However, it is found that this scheme needs extra artificial dissipation to maintain the numerical stability. Hu et al. [21] developed a 6th-order central-upwind WENO scheme which is analogous to the scheme [20] but with a different smoothness indicator for the downwind stencil and no additional artificial dissipation is needed.

* Corresponding author.
E-mail addresses: wangyh14@lsec.cc.ac.cn (Y. Wang), klzhao@lsec.cc.ac.cn (K. Zhao), lyuan@lsec.cc.ac.cn (L. Yuan).

https://doi.org/10.1016/j.compfluid.2020.104625
0045-7930/

More recently, Hu [22] found that the 6th-order WENO scheme [21] generates evident oscillations around discontinuities for CFL number greater than 0.6, and the oscillations grow with increasing grid points. Hu [22] fixed this problem by letting the most downwind stencil to include an upwind point so as to increase numerical stability. A direct use of the Jiang-Shu nonlinear weights makes the resulting scheme achieve only 5th-order accuracy in smooth regions of the solution without critical points. Two strategies were used in [22] to recover the optimal order of accuracy. One is the mapping function [12,23,24], another is the reference smoothness indicator [13,21]. The latter strategy has less computational cost and can obtain nearly identical results to the first one.

In this work, we further improve upon the 6th-order WENO scheme of Hu [22] to enhance the resolution while maintaining the robustness and efficiency. The most upwind stencil is modified to be composed of 4 grid points, while the inner two stencils still use 3 grid points but the reconstructions are made 4th-order accurate by adding cubic correction terms involving the global five grid points of the classical WENO scheme as did in [18]. We compute the smoothness indicator of each stencil according to the Jiang-Shu formula [5]. However, the resulting Jiang-Shu weights can not satisfy the sufficient condition for ensuring the optimal order of convergence, and the scheme achieves only 5th-order accuracy in smooth regions. To recover the optimal order, we use a reference global smoothness indicator to construct a WENO-Z type scheme (called WENO-MSZ6 where MS stands for “Modified Stencil”). Several numerical examples show that the WENO-MSZ6 scheme achieves 6th-order accuracy in smooth regions including the first order critical points and has small dissipation errors while maintaining the robustness and efficiency of the recently developed 6th-order WENO schemes [21,22].

The organization of this paper is as follows. In Section 2, the recently developed 6th-order WENO schemes are reviewed. In Section 3, we present a new modified 6th-order WENO scheme using a reference smoothness indicator to recover the optimal order. Section 4 presents several benchmark examples to demonstrate the performance of the new scheme. A conclusion is given in Section 5.

2. The 6th-order central-upwind WENO schemes

In this section, we briefly review two similar and most recent 6th-order central-upwind finite difference WENO schemes, i.e., WENO-CU6 [21] and WENO-Z6 [22] for solving the one-dimensional hyperbolic conservation law

$$u_t + f(u)_x = 0, \quad a \le x \le b, \quad t > 0, \tag{1}$$

where $u(x, t)$ is the conservative variable, $f(u(x, t))$ is the flux function. Eq. (1) is solved on a uniform grid defined by the nodes $x_i = a + (i-0.5)\Delta x, i = 1, \cdots, N$, which are also called cell centers, with cell interfaces given by $x_{i+1/2} = x_i + \Delta x/2$, where $\Delta x = (b-a)/N$ is the grid spacing. Throughout this paper, a function value at the center x_i is denoted by a subscript i, e.g., $f_i = f(x_i)$.

The spatial derivative in Eq. (1) can be approximated by a conservative finite difference between cell boundaries, giving the semi-discretization form

$$\frac{du_i}{dt} = -\frac{h_{i+\frac{1}{2}} - h_{i-\frac{1}{2}}}{\Delta x}, \tag{2}$$

where $u_i(t)$ is the numerical approximation to the point value $u(x_i, t)$ at the node x_i, and $h(x)$ is a numerical flux function defined implicitly as [25]

$$f(x) = \frac{1}{\Delta x}\int_{x-\Delta x/2}^{x+\Delta x/2} h(\xi)d\xi. \tag{3}$$

If $h_{i\pm1/2}$ in (2) are approximated by numerical fluxes $\hat{f}_{i\pm1/2}$ reconstructed from known cell average values f_i, i.e., $\hat{f}_{i\pm1/2} = h_{i\pm1/2} + \mathcal{O}(\Delta x^6)$, and the $\mathcal{O}(\Delta x^6)$ term is smooth, then Eq. (2) will have $\mathcal{O}(\Delta x^6)$ accuracy.

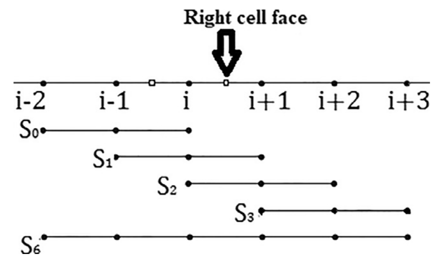

Fig. 1. Stencils of the WENO-CU6 scheme [21] for the numerical flux $\hat{f}_{i+1/2}$. For the WENO-Z6 scheme [22], the stencil S_3 has an extra upwind point i.

The 6th-order WENO schemes [21,22] use the characteristic-wise decomposition and local Lax-Friedrichs flux splitting techniques for the WENO reconstruction as in [26]. Hereafter, we will only describe the construction of the positive numerical flux in a characteristic component as formulas for the negative numerical flux are symmetric about the grid interface $x_{i+1/2}$. For simplicity we will drop the “ + ” sign in the superscript of the positive flux f^+.

2.1. Review of the construction of the WENO-CU6 and WENO-Z6 schemes

The 6th-order central-upwind WENO scheme (WENO-CU6) [21] use a 6-point global stencil S_6 which is subdivided into four candidate stencils as shown in Fig. 1. They differ from the classical 5th-order WENO scheme in a downwind point $i+3$ and a downwind stencil S_3. Also, the stencil S_3 for the WENO-Z6 scheme [22] has an additional upwind point which may help numerical stability. Candidate numerical fluxes at the grid interface $i+1/2$ are calculated and a convex combination of the four candidate numerical fluxes $\hat{f}^{(k)}_{i+1/2}, k = 0, 1, 2, 3$ gives the numerical flux with the optimal weights to retain the 6th-order accuracy in smooth regions. However, in order to suppress spurious oscillations near discontinuities, the weights should effectively remove the contribution of stencils which contain the discontinuity. To be more specific, let

$$S_k = \{i+k-2, i+k-1, i+k\}, \quad k = 0, 1, 2, 3$$

and

$$S_k = \{i+k-2, i+k-1, i+k\}, \quad k = 0, 1, 2,$$
$$S_3 = \{i, i+1, i+2, i+3\}$$

be the four candidate stencils of the WENO-CU6 [21] and WENO-Z6 [19] schemes, respectively.

To approximate the function $h(x)$ in Eq. (2), 2nd-degree polynomials $\hat{f}^{(k)}(x) = a_{0,k} + a_{1,k}x + a_{2,k}x^2$ are constructed on all candidate stencils except S_3 of the WENO-Z6 scheme where a 3rd-degree polynomial is constructed. The coefficients of the polynomials are calculated according to Eq. (3) with known values of f_i at stencil nodes. Each $\hat{f}^{(k)}(x)$ calculated gives a 3rd-order (or 4th-order on S_3 of WENO-Z6) approximation of $h(x)$. Evaluations of $\hat{f}^{(k)}(x)$ at the $i+1/2$ grid interface give the candidate fluxes

$$\hat{f}^0_{i+1/2} = \frac{1}{3}f_{i-2} - \frac{7}{6}f_{i-1} + \frac{11}{6}f_i,$$
$$\hat{f}^1_{i+1/2} = -\frac{1}{6}f_{i-1} + \frac{5}{6}f_i + \frac{1}{3}f_{i+1},$$
$$\hat{f}^2_{i+1/2} = \frac{1}{3}f_i + \frac{5}{6}f_{i+1} - \frac{1}{6}f_{i+2},$$
$$\hat{f}^3_{i+1/2} = \frac{11}{6}f_{i+1} - \frac{7}{6}f_{i+2} + \frac{1}{3}f_{i+3} \quad \text{(WENO-CU6)},$$

$$\hat{f}^3_{i+1/2} = \frac{1}{4}f_i + \frac{13}{12}f_{i+1} - \frac{5}{12}f_{i+2} + \frac{1}{12}f_{i+3} \quad \text{(WENO-Z6)}, \tag{4}$$

where the last two equations are contributions of the downwind stencil S_3. A nonlinear convex combination of $\hat{f}^k_{i+1/2}$ on the four stencils is used to define the WENO numerical flux

$$\hat{f}_{i+1/2} = \sum_{k=0}^{3} \omega_k \hat{f}^k_{i+1/2}. \tag{5}$$

To construct the nonlinear weights ω_k in Eq. (5), the four optimal weights $d_k, k = 0, 1, 2, 3$ are needed. The optimal weights d_k are found such that their linear combination with the four candidate fluxes, $\sum_{k=0}^{3} d_k \hat{f}^k_{i+1/2}$, recovers the optimal 6th-order approximation of the smooth function $h(x)$

$$\begin{aligned} \hat{f}_{i+1/2} &= \frac{1}{60}(f_{i-2} - 8f_{i-1} + 37f_i + 37f_{i+1} - 8f_{i+2} + f_{i+3}) \\ &= h_{i+1/2} + \mathcal{O}(\Delta x^6). \end{aligned} \tag{6}$$

By using Eq. (4) and direct algebraic calculation, one gets the linear optimal weights

$$d_0 = \frac{1}{20},\ d_1 = \frac{9}{20},\ d_2 = \frac{9}{20},\ d_3 = \frac{1}{20}, \quad \text{(WENO-CU6)} \tag{7}$$

$$d_0 = \frac{1}{20},\ d_1 = \frac{9}{20},\ d_2 = \frac{6}{20},\ d_3 = \frac{4}{20}, \quad \text{(WENO-Z6)} \tag{8}$$

The nonlinear weights ω_k take a form similar to the WENO-Z scheme [13],

$$\omega_k = \frac{\alpha_k}{\sum_{l=0}^{3} \alpha_l}, \quad \alpha_k = d_k\left(C + \frac{\tau_6}{\beta_k + \epsilon}\right), \tag{9}$$

where $\epsilon = 10^{-40}$, $k = 0, 1, 2, 3$. The WENO-CU6 scheme introduces a free parameter $C \gg 1$ to increase the contribution of the optimal weights when the smoothness indicators have comparable magnitudes inspired by the work [27]. However, the WENO-Z6 scheme uses $C = 1$ in order to avoid numerical oscillations around discontinuities for large CFL number associated with $C \gg 1$.

The first three smoothness indicators β_k in Eq. (9) are defined as [26]

$$\beta_k = \sum_{l=1}^{2} \int_{x_{i-1/2}}^{x_{i+1/2}} \Delta x^{2l-1} \left(\frac{d^l}{dx^l}\hat{f}^{(k)}\right)^2 dx, \quad k = 0, 1, 2. \tag{10}$$

However, the fourth smoothness indicator β_3 in the WENO-CU6 scheme is defined to be that of the 6-point stencil for the 6th-order interpolation

$$\beta_3 = \beta_6 = \sum_{l=1}^{5} \int_{x_{i-1/2}}^{x_{i+1/2}} \Delta x^{2l-1} \left(\frac{d^l}{dx^l}\hat{f}^{(6)}\right)^2 dx. \tag{11}$$

Eq. (10) has the well-known form:

$$\begin{aligned} \beta_0 &= \beta_0^{JS} = \frac{1}{4}(f_{i-2} - 4f_{i-1} + 3f_i)^2 + \frac{13}{12}(f_{i-2} - 2f_{j-1} + f_i)^2, \\ \beta_1 &= \beta_1^{JS} = \frac{1}{4}(f_{i-1} - f_{i+1})^2 + \frac{13}{12}(f_{i-1} - 2f_i + f_{i+1})^2, \\ \beta_2 &= \beta_2^{JS} = \frac{1}{4}(3f_i - 4f_{i+1} + f_{i+2})^2 + \frac{13}{12}(f_i - 2f_{i+1} + f_{i+2})^2. \end{aligned} \tag{12}$$

Eq. (11) takes the specific form [21]

$$\begin{aligned} \beta_3 = \beta_6 = \frac{1}{10080}\big[& 271779 f_{i-2}^2 + f_{i-2}(2380800 f_{i-1} + 4086352 f_i \\ & - 3462252 f_{i+1} + 1458762 f_{i+2} - 245620 f_{i+3}) \\ & + f_{i-1}(5653317 f_{i-1} - 20427884 f_i + 17905032 f_{i+1} \\ & - 7727988 f_{i+2} + 1325006 f_{i+3}) \\ & + f_i(19510972 f_i - 35817664 f_{i+1} + 15929912 f_{i+2} \\ & - 2792660 f_{i+3}) \\ & + f_{i+1}(17195652 f_{i+1} - 15880404 f_{i+2} + 2863984 f_{i+3}) \\ & + f_{i+2}(3824847 f_{i+2} - 1429976 f_{i+3}) + 139633 f_{i+3}^2)\big] \end{aligned} \tag{13}$$

The fourth smoothness indicator β_3 in the WENO-Z6 scheme is still defined to be the Jiang-Shu smoothness indicator based on the local stencil interpolation

$$\begin{aligned} \beta_3 &= \sum_{l=1}^{3} \int_{x_{i-1/2}}^{x_{i+1/2}} \Delta x^{2l-1} \left(\frac{d^l}{dx^l}\hat{f}^{(3)}\right)^2 dx \\ &= \frac{1}{36}(11f_i - 18f_{i+1} + 9f_{i+2} - 2f_{i+3})^2 \\ &\quad + \frac{13}{12}(2f_i - 5f_{i+1} + 4f_{i+2} - f_{i+3})^2 \\ &\quad + \frac{781}{720}(f_i - 3f_{i+1} + 3f_{i+2} - f_{i+3})^2. \end{aligned} \tag{14}$$

Finally, the reference smoothness indicator τ_6 is defined by Hu et al [21]

$$\tau_6 = \left|\beta_3 - \frac{1}{6}(\beta_0 + 4\beta_1 + \beta_2)\right| = \begin{cases} \mathcal{O}(\Delta x^6) & \text{(WENO-CU6)} \\ \mathcal{O}(\Delta x^5) & \text{(WENO-Z6)} \end{cases}. \tag{15}$$

Remark 1. The WENO-CU6 scheme would have only 4th order in smooth region without critical point if using the classic WENO-JS weights [5]. It achieves the optimal 6th-order accuracy by using the WENO-Z weights (9), but it still degenerates to 4th-order even 2nd-order accuracy at critical points. The smoothness indicator β_3 over the 6-point global stencil is meant to weight the three upwind stencils and the downwind stencil. However, the scheme produces evident spurious oscillations for large CFL number due to a large parameter C.

Remark 2. The WENO-Z6 scheme would have only 5th order in smooth region without critical point if using the classic WENO-JS weights [5]. It achieves 6th-order accuracy by using the WENO-Z weights (9) with $C = 1$. However, it still loses one order of accuracy at critical points. This scheme produces comparable results with the WENO-CU6 scheme, but has less computational cost, and tolerates large CFL number without producing oscillations.

3. Construction of a new 6th-order WENO scheme

In this section, we present a new 6th-order WENO scheme. As with previous 6th-order WENO schemes [19,21,22], we also use four stencils for calculating the numerical flux $\hat{f}_{i+1/2}$ as shown in Fig. 2. The stencils S_k are composed of different numbers of nodes, specifically,

$$\begin{aligned} & S_0 = \{i-2, i-1, i, i+1\},\ S_1 = \{i-1, i, i+1\}, \\ & S_2 = \{i, i+1, i+2\}, \\ & S_3 = \{i, i+1, i+2, i+3\}, \end{aligned} \tag{16}$$

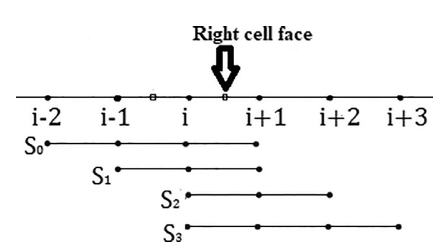

Fig. 2. Stencils of the present WENO-MSZ6 scheme for the numerical flux $\hat{f}_{i+1/2}$.

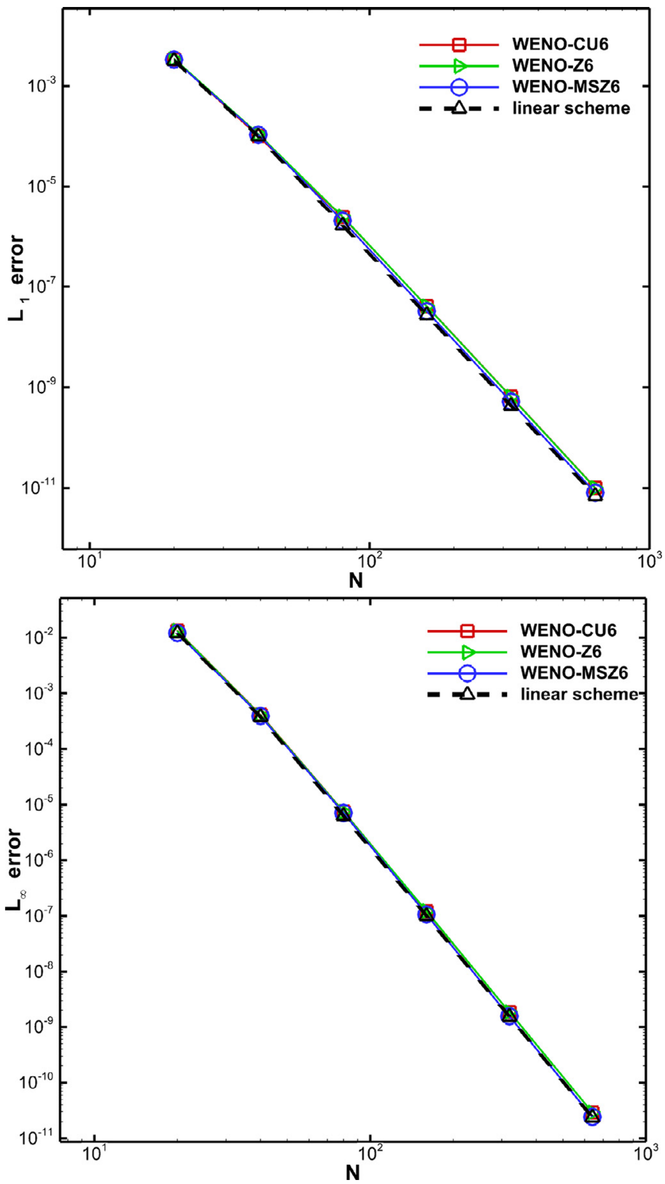

Fig. 3. The L_1 (top) and L_∞ (bottom) errors computed with the WENO-CU6, WENO-Z6, WENO-MSZ6 and linear schemes, respectively, for the linear advection Eq. (32) with the initial condition (33) at $t = 2.0$.

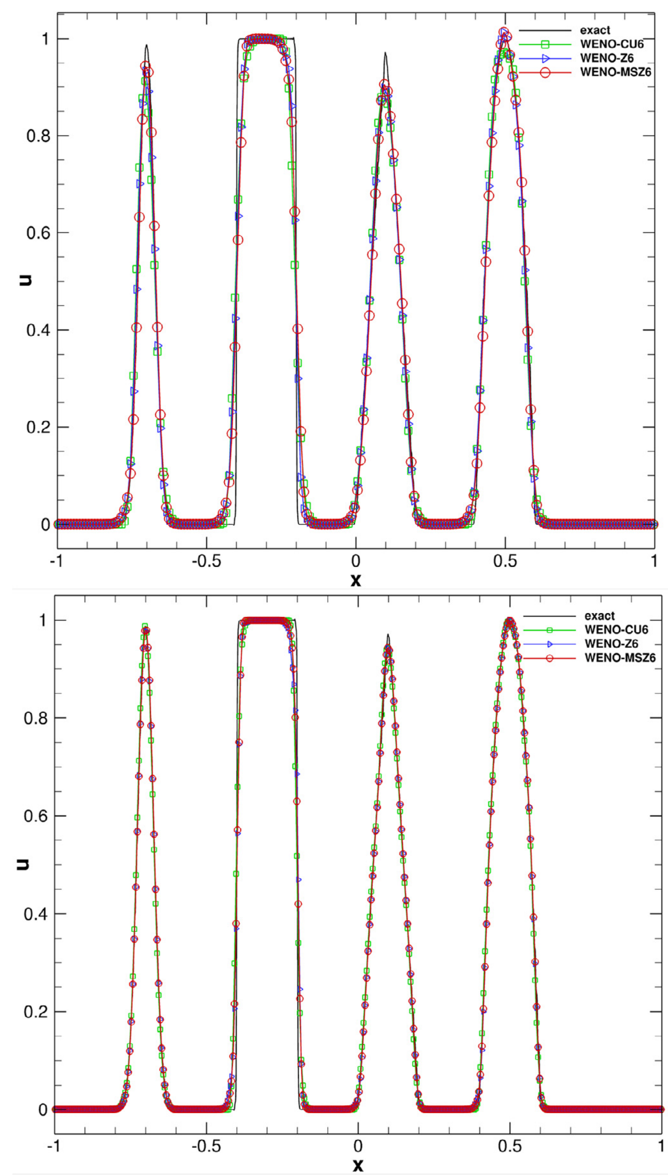

Fig. 4. Comparison between the exact and numerical solutions of the linear advection Eq. (32) with the initial condition (34) by using WENO-CU6, WENO-Z6, WENO-MSZ6 at $t = 6$ with 200 (top) and 400 grid points (bottom).

where S_0 has an extra point $i+1$. For the two nominally 3-point stencils S_1 and S_2, we add cubic correction terms to the original 2nd-degree polynomial interpolations such that the results become 4th-order approximations as did in our previous paper [18]. These correction terms depend on 5 points from $i-2$ to $i+2$ as the classic WENO scheme [5]. For the two 4-point stencils S_0 and S_4, we use the same 3rd-degree polynomial interpolations as [22]. Thus for the four stencils S_k, $k = 0, 1, 2, 3,$ we construct candidate flux polynomials $\hat{f}^{(k)}(x)$ which are 4th-order approximations to the implicit function $h(x)$, and evaluate them at the interface $i+1/2$ to give

$$\hat{f}^0_{i+1/2} = \frac{1}{12}f_{i-2} - \frac{5}{12}f_{i-1} + \frac{13}{12}f_i + \frac{1}{4}f_{i+1},$$

$$\hat{f}^1_{i+1/2} = -\frac{1}{6}f_{i-1} + \frac{5}{6}f_i + \frac{1}{3}f_{i+1} - \frac{1}{24}(-f_{i-2} + 2f_{i-1} - 2f_{i+1} + f_{i+2}),$$

$$\hat{f}^2_{i+1/2} = \frac{1}{3}f_i + \frac{5}{6}f_{i+1} - \frac{1}{6}f_{i+2} + \frac{1}{24}(-f_{i-2} + 2f_{i-1} - 2f_{i+1} + f_{i+2}),$$

$$\hat{f}^3_{i+1/2} = \frac{1}{4}f_i + \frac{13}{12}f_{i+1} - \frac{5}{12}f_{i+2} + \frac{1}{12}f_{i+3}. \tag{17}$$

The linear convex combination of the four candidate fluxes, $\sum_{k=0}^{3} d_k \hat{f}^k_{i+1/2}$, should recover the optimal 6th-order numerical flux (6). By using Eq. (17) and by direct algebraic calculation, we can get the linear optimal weights

$$d_0 = \frac{1}{5},\ d_1 = \frac{3}{10},\ d_2 = \frac{3}{10},\ d_3 = \frac{1}{5}. \tag{18}$$

Following the idea of the conventional WENO schemes, a nonlinear convex combination of the candidate numerical fluxes $\hat{f}^k_{i+1/2}$ (17)

$$\hat{f}^{MS}_{i+1/2} = \omega_0 \hat{f}^0_{i+1/2} + \omega_1 \hat{f}^1_{i+1/2} + \omega_2 \hat{f}^2_{i+1/2} + \omega_3 \hat{f}^3_{i+1/2} \tag{19}$$

is used to compute the numerical flux, where MS denotes “modified stencil”. The nonlinear weights ω_k in Eq. (19) can be defined

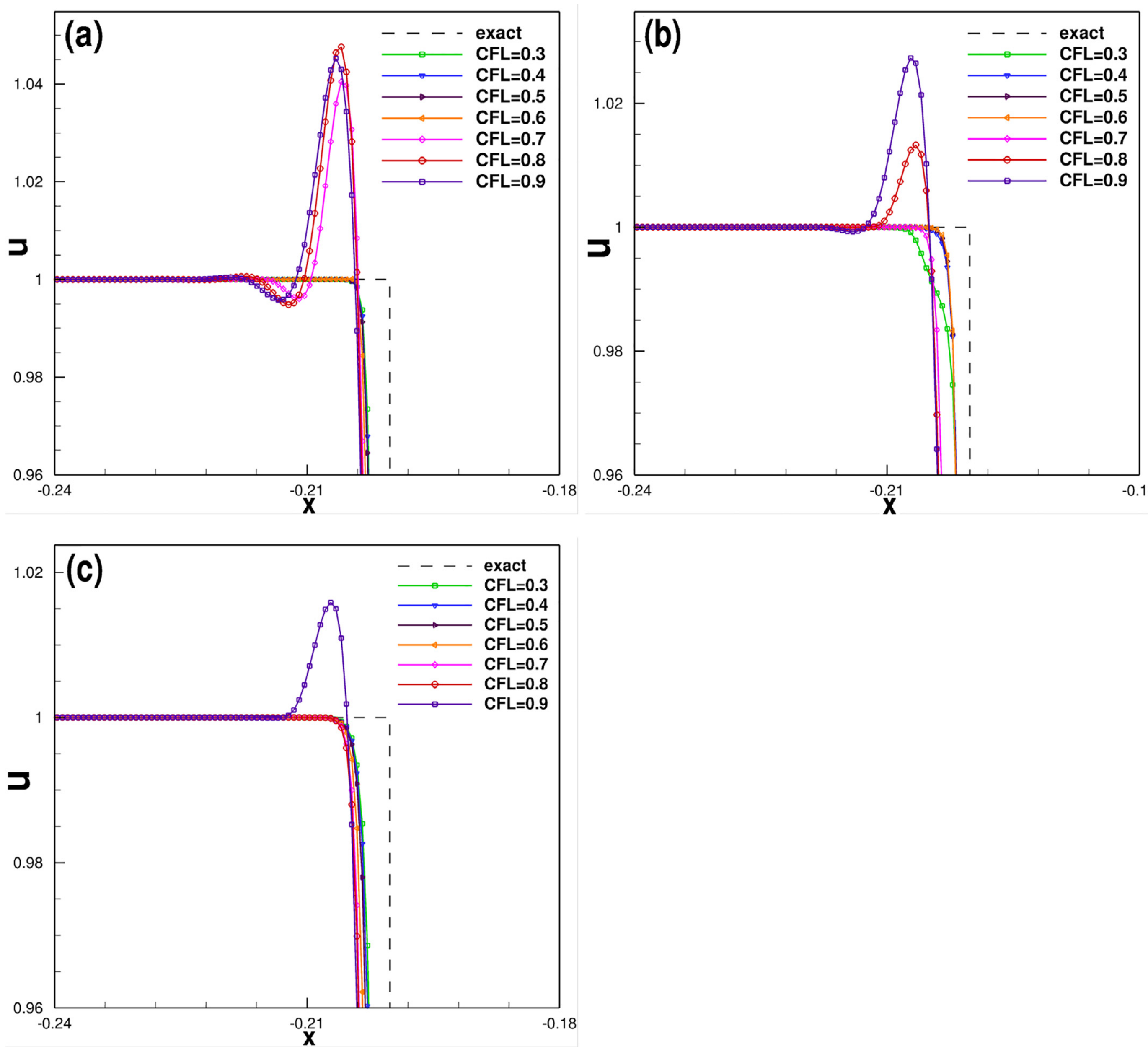

Fig. 5. Local view of numerical solutions of the linear advection Eq. (32) with the initial condition (34) with $N = 3200$ by using (a) WENO-CU6, (b) WENO-Z6, (c) WENO-MSZ6.

using the JS-weights [5]

$$\omega_k = \frac{\alpha_k}{\sum_{l=0}^{3} \alpha_l}, \quad \alpha_k = \frac{d_k}{(\beta_k + \epsilon)^2}, \quad k = 0, 1, 2, 3. \tag{20}$$

The smoothness indicators β_k are calculated according to the conventional formula [5,26], which have the discrete form

$$\begin{aligned}
\beta_0 &= \frac{1}{36}(2f_{i-2} - 9f_{i-1} + 18f_i - 11f_{i+1})^2 \\
&\quad + \frac{13}{12}(f_{i-2} - 4f_{i-1} + 5f_i - 2f_{i+1})^2 \\
&\quad + \frac{781}{720}(f_{i-2} - 3f_{i-1} + 3f_i - f_{i+1})^2, \\
\beta_1 &= \frac{1}{4}(f_{i-1} - f_{i+1})^2 + \frac{13}{12}\left(f_{i-1} - 2f_j + f_{i+1}\right)^2 \\
&\quad + \frac{89}{320}(-f_{i-2} + 2f_{i-1} - 2f_{i+1} + f_{i+2})^2 \\
&\quad + \frac{1}{12}\left(-f_{i-2} + 2f_{i-1} - 2f_{i+1} + f_{j+2}\right)(f_{i-1} - f_{i+1}), \\
\beta_2 &= \frac{1}{4}(3f_i - 4f_{i+1} + f_{i+2})^2 + \frac{13}{12}(f_i - 2f_{i+1} + f_{i+2})^2 \\
&\quad + \frac{547}{960}(-f_{i-2} + 2f_{i-1} - 2f_{i+1} + f_{i+2})^2 \\
&\quad - \frac{1}{12}\left(-f_{i-2} + 2f_{i-1} - 2f_{i+1} + f_{j+2}\right) \\
&\quad \times (19f_i - 34f_{i+1} + 15f_{i+2}), \\
\beta_3 &= \frac{1}{36}(11f_i - 18f_{i+1} + 9f_{i+2} - 2f_{i+3})^2 \\
&\quad + \frac{13}{12}(2f_i - 5f_{i+1} + 4f_{i+2} - f_{i+3})^2 \\
&\quad + \frac{781}{720}(f_i - 3f_{i+1} + 3f_{i+2} - f_{i+3})^2.
\end{aligned} \tag{21}$$

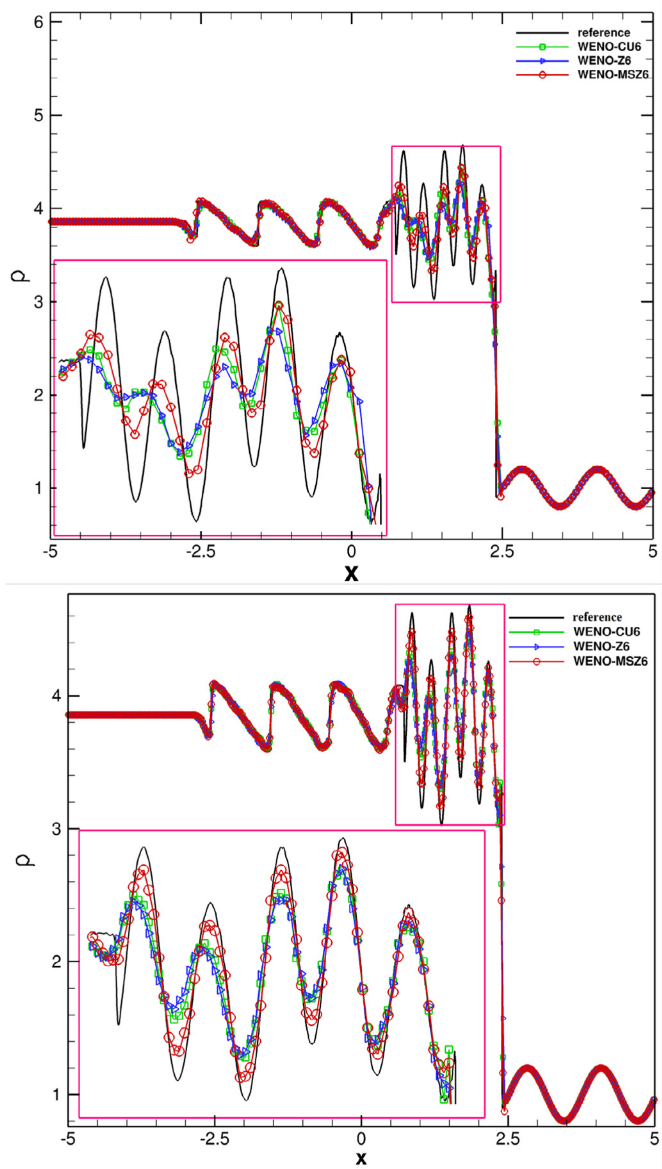

Fig. 6. Density profiles of the shock-entropy wave interaction [23] with WENO-CU6, WENO-Z6 and WENO-MSZ6 at $t = 1.8$ with 200 (top) and 400 grid points (bottom).

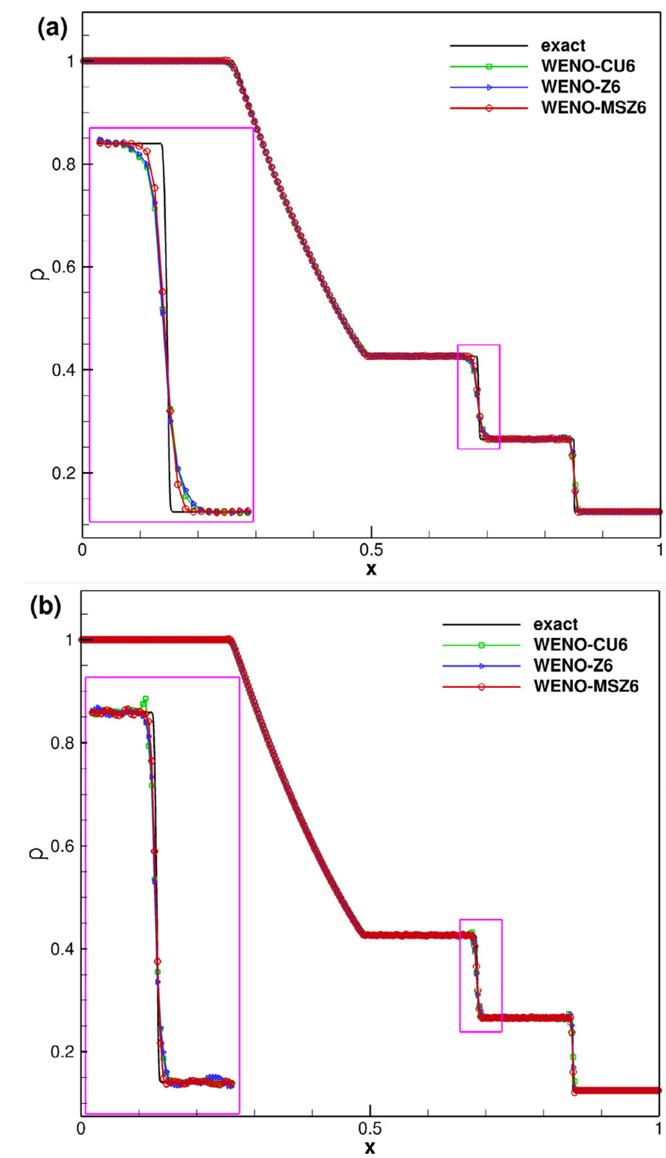

Fig. 7. Density profiles of shock tube problem computed with WENO-CU6, WENO-Z6 and WENO-MSZ6 at $t = 0.2$. (a) 200 grid points with CFL $= 0.6$. (b) 400 grid points with CFL $= 0.8$.

Here, β_0 and β_3 are the same as in the WENO-Z6 scheme [22], and β_1 and β_2 are the same as in our modified stencil 5th-order WENO scheme [18]. Eqs. (17)–(21) constitute our naively modified 6th-order WENO scheme.

Remark 3. In practical use, we define a tunable function φ as in [18]

$$\varphi = 1 - \left(\frac{|\beta_0^{\mathrm{JS}} - \beta_2^{\mathrm{JS}}|}{\beta_0^{\mathrm{JS}} + \beta_2^{\mathrm{JS}} + \epsilon} \right)^r, \quad r \geq 1, \tag{22}$$

and multiply φ with the last two terms in β_1 and β_2 in (21) and the last terms in $\hat{f}^1_{i+1/2}$ and $\hat{f}^2_{i+1/2}$ in (17) in order to suppress numerical oscillations associated with these terms. ϵ is a small positive number used to avoid division by zero. This φ does not affect the optimal order of convergence [18]. We take $r = 1$.

In the following two subsections, we first analyse the accuracy of the naively modified 6th-order WENO scheme, then apply a remedy method to the scheme to recover the optimal 6th-order accuracy in smooth region including the first-order critical point.

3.1. Accuracy analysis of the naively modified 6th-order WENO scheme

First, we can derive a sufficient condition for 6th-order convergence of Eq. (19). Adding and subtracting $\sum_{k=0}^{3} d_k \hat{f}^k_{i+1/2}$ from Eq. (19) give

$$\hat{f}_{i+1/2} = \sum_{k=0}^{3} d_k \hat{f}^k_{i+1/2} + \sum_{k=0}^{3} (\omega_k - d_k) \hat{f}^k_{i+1/2}, \tag{23}$$

where the first term on the right-hand-side produces the 6th-order accurate numerical flux (6). The second term must be at least $\mathcal{O}(\Delta x^7)$ in order for $(\hat{f}_{i+1/2} - \hat{f}_{i-1/2})/\Delta x$ to be approximated at sixth order. Noting that the $\hat{f}^k_{i+1/2}$ (17) are 4th-order approxima-

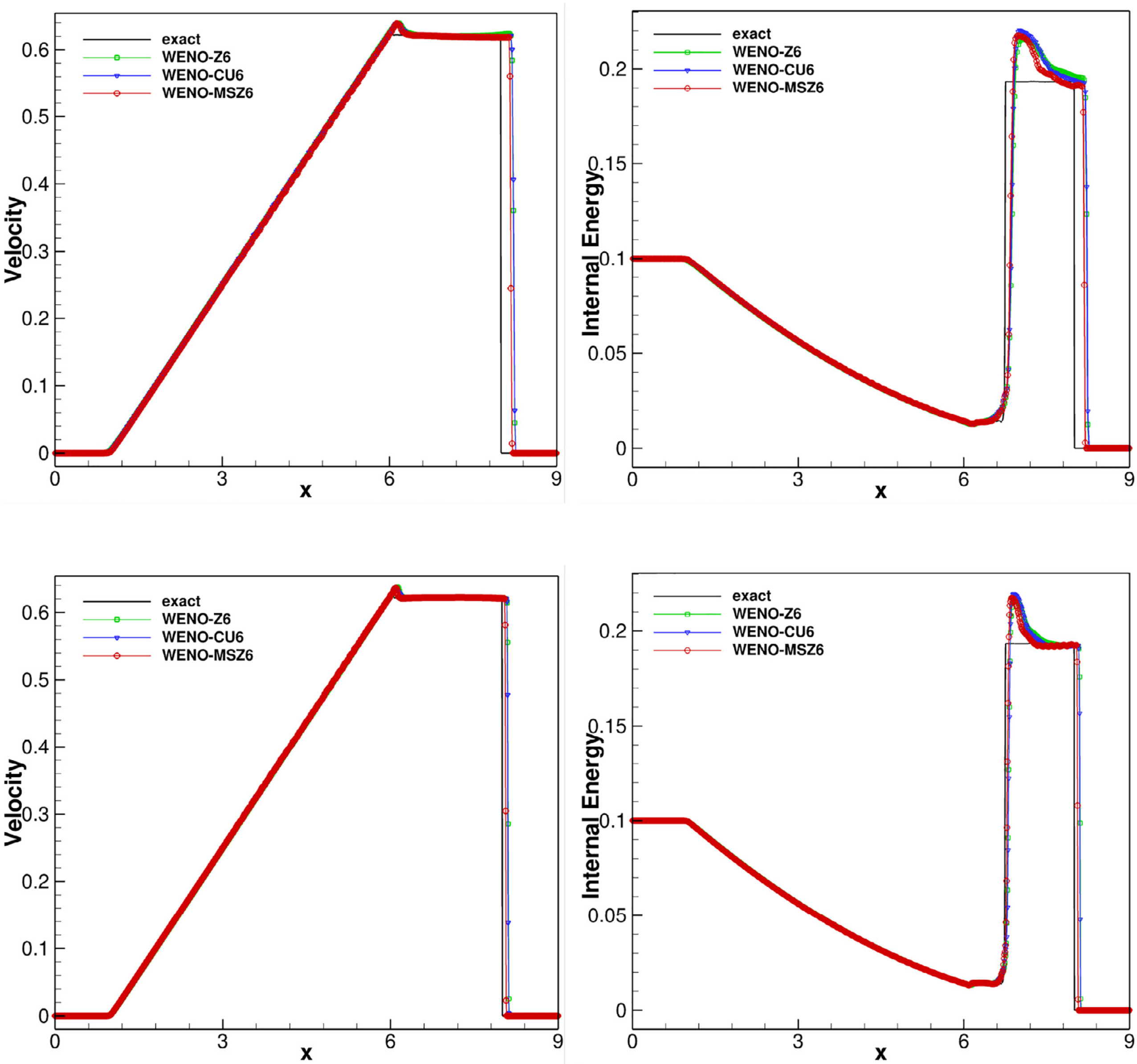

Fig. 8. Velocity and internal energy profiles of the LeBlanc shock tube problem [30,31] computed with the WENO-CU6, WENO-Z6 and WENO-MSZ6 schemes at $t = 6$ with CFL = 0.6 on 400 grid points (top), and 800 grid points (bottom).

tions of $h_{i+1/2}$, we have

$$\sum_{k=0}^{3}(\omega_k - d_k)\tilde{f}^k_{i+1/2} = \sum_{k=0}^{3}(\omega_k - d_k)\big(h_{i+1/2} + \mathcal{O}\big(\Delta x^4\big)\big)$$
$$= h_{i+1/2}\sum_{k=0}^{3}(\omega_k - d_k) + \sum_{k=0}^{3}(\omega_k - d_k)\mathcal{O}(\Delta x^4), \tag{24}$$

where the first term on the right-hand-side vanishes due to the normalization of the weights. Thus, it is sufficient to require

$$\omega_k = d_k + \mathcal{O}(\Delta x^3) \tag{25}$$

for the overall scheme to have 6th-order accuracy. We remark that the sufficient condition (25) relaxes the requirement on the weights by one order compared with that in [21,22] due to the present 4th-order stencil approximations.

Second, Taylor-series expansions of the smoothness indicator (21) at point i give

$$\beta_0 = f_i'^2\Delta x^2 + \frac{13}{12}f_i''^2\Delta x^4 + \frac{1}{2}f_i' f^{(4)}\Delta x^5 + \mathcal{O}(\Delta x^6),$$
$$\beta_1 = f_i'^2\Delta x^2 + \frac{13}{12}f_i''^2\Delta x^4 + \mathcal{O}(\Delta x^6),$$
$$\beta_2 = f_i'^2\Delta x^2 + \frac{13}{12}f_i''^2\Delta x^4 - \frac{1}{2}f_i' f_i^{(4)}\Delta x^5 + \mathcal{O}(\Delta x^6),$$
$$\beta_3 = f_i'^2\Delta x^2 + \frac{13}{12}f_i''^2\Delta x^4 + \frac{1}{2}f_i' f_i^{(4)}\Delta x^5 + \mathcal{O}(\Delta x^6). \tag{26}$$

Following the analysis in [12], Eq. (26) can be written as

$$\beta_k = D\big(1 + \mathcal{O}(\Delta x^2)\big). \tag{27}$$

where D is some non-zero constant independent of k. Notice that Eq. (27) holds even for $f_i' = 0, f_i'' \neq 0$. Substitution of Eq. (27) into

Eq. (20) gives

$$\omega_k = d_k + \mathcal{O}(\Delta x^2). \tag{28}$$

Comparison of this result with the condition (25) shows that the naively modified 6th-order WENO scheme actually achieves only 5th-order accuracy in smooth regions. To recover the optimal order of accuracy, we should make the nonlinear weights approximate the linear weights with $\mathcal{O}(\Delta x^3)$.

In the following subsection, we use the strategy of reference smoothness indicator [13] to recover the optimal 6th-order accuracy.

3.2. A reference smoothness indicator to recover the optimal 6th-order accuracy

The nonlinear weights can be computed as per the WENO-Z scheme [13] by

$$\omega_k^Z = \frac{\alpha_k^Z}{\sum_{l=0}^{3} \alpha_l^Z}, \quad \alpha_k^Z = d_k\left(1 + \left(\frac{\tau_6}{\beta_k + \epsilon}\right)^p\right), \quad k = 0, \ldots, 3, \tag{29}$$

where the parameter p is used to control the order of accuracy and dissipation. In Ref. [22] $p = 1$ attains the optimal order in smooth region without critical point while $p = 2$ attains the optimal order even at critical point but increases the dissipation. Since the reference smoothness indicator τ_6 is preferred to contain all 6 points, the highest order we can obtain from the expansions (26) is the following linear combination which is slightly different from Eq. (15):

$$\tau_6 = |\beta_3 - \beta_0| = \mathcal{O}(\Delta x^6). \tag{30}$$

For $p = 1$, through simple computation, we get

$$\omega_k^Z = d_k + \mathcal{O}(\Delta x^4), \quad k = 0, 1, 2, 3, \tag{31}$$

which obviously satisfy the sufficient condition (25) in smooth region including the first-order critical point ($f_i' = 0, f_i'' \neq 0$). We call the modified 6th-order WENO scheme with the weights (29) ($p = 1$) "WENO-MSZ6" scheme, where MS represents "Modified Stencil".

4. Numerical tests

In this section, we provide several numerical examples to demonstrate the performance of the proposed WENO-MSZ6 scheme. The numerical results are compared with the 6th-order WENO-CU6 [21] with $C = 20$ in Eq. (9) and the WENO-Z6 [22] schemes. $\epsilon = 10^{-40}$ is used in Eqs. (9), (22) and (29). The presentation of this section starts with problems for the linear advection equation, followed by problems for the 1D and 2D Euler equations and 2D Navier-Stokes equations. The characteristic decomposition and local Lax-Friedrichs flux splitting techniques for systems are used in the WENO reconstruction [26]. The time integration is carried out with the third-order TVD Runge-Kutta method [28,29].

4.1. Linear advection problems

In this subsection, we test the new scheme in the 1D scalar linear advection equation with periodic boundary conditions,

$$u_t + u_x = 0, \quad -1 \leq x \leq 1, \quad t \geq 0. \tag{32}$$

We consider two initial conditions. The first initial condition

$$u(x, 0) = \sin\left(\pi x - \frac{\sin(\pi x)}{\pi}\right) \tag{33}$$

is used to test the order of convergence. The solution of Eq. (32) with the initial condition (33) has two critical points at

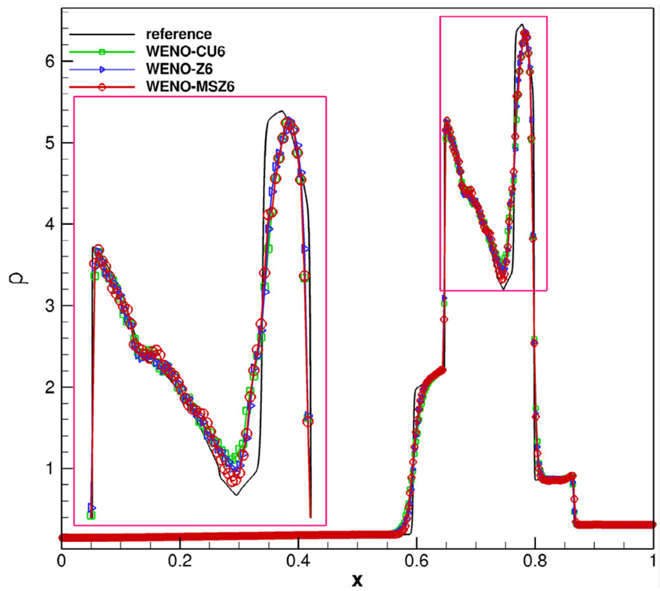

Fig. 9. Density profiles of the interacting blast waves [24] computed with the WENO-CU6,WENO-Z6 and WENO-MSZ6 schemes at $t = 0.038$ with CFL= 0.6 on 400 grid points. The zoom is near the contact discontinuity.

Table 1
CPU time (seconds) of different schemes spent for interacting blast waves.

N	WENO-Z6	WENO-CU6	WENO-MSZ6
100	0.223	0.247	0.263
400	2.901	3.132	3.287
1600	39.634	40.865	41.641

$x \approx \pm 0.59$ [12]. The time step is taken as $\Delta t = \Delta x^2$ so that the 3rd-order TVD Runge-Kutta method in time is effectively 6th-order. This problem is computed on different grids with $N = 20$, 40, 80, 160, 320 and 640 grid cells. Fig. 3 shows the L_1 and L_∞ errors at $t = 2$. The norm of the error is computed by comparison with the exact solution according to

$$L_1 = \Delta x \sum_{i=1}^{N} |u_i - u_{\text{exact},i}|,$$

$$L_\infty = \max |u_i - u_{\text{exact},i}| \quad \forall\ i = 1, \ldots, N.$$

We see that the three 6th-order WENO schemes have almost the same errors as the linear central 6th-order scheme and converge with 6th-order accuracy.

The second initial condition, which contains a Gaussian, a square wave, a triangle and a semi-ellipse wave, is given by

$$u(x, 0) = \begin{cases} \frac{1}{6}(G(x, \beta, z - \delta) + G(x, \beta, z + \delta) & \\ +4G(x, \beta, z)), & -0.8 \leq x \leq -0.6, \\ 1.0, & -0.4 \leq x \leq -0.2, \\ 1 - |10(x - 0.1)|, & 0.0 \leq x \leq 0.2, \\ \frac{1}{6}(F(x, \alpha, a - \delta) + G(x, \alpha, a + \delta) & \\ +4G(x, \alpha, a)), & 0.4 \leq x \leq 0.6, \\ 0.0, & \text{otherwise}. \end{cases} \tag{34}$$

where $G(x, \beta, z) = \exp^{-\beta(x-z)^2}$, $F(x, \alpha, a) = \sqrt{\max(1 - \alpha^2(x - a)^2, 0)}$, $a = 0.5$, $z = -0.7$, $\delta = 0.005$, $\alpha = 10$ and $\beta = \ln 2/36\delta^2$. The solution of Eq. (32) with the initial condition (34) consists of discontinuities, corner singularities

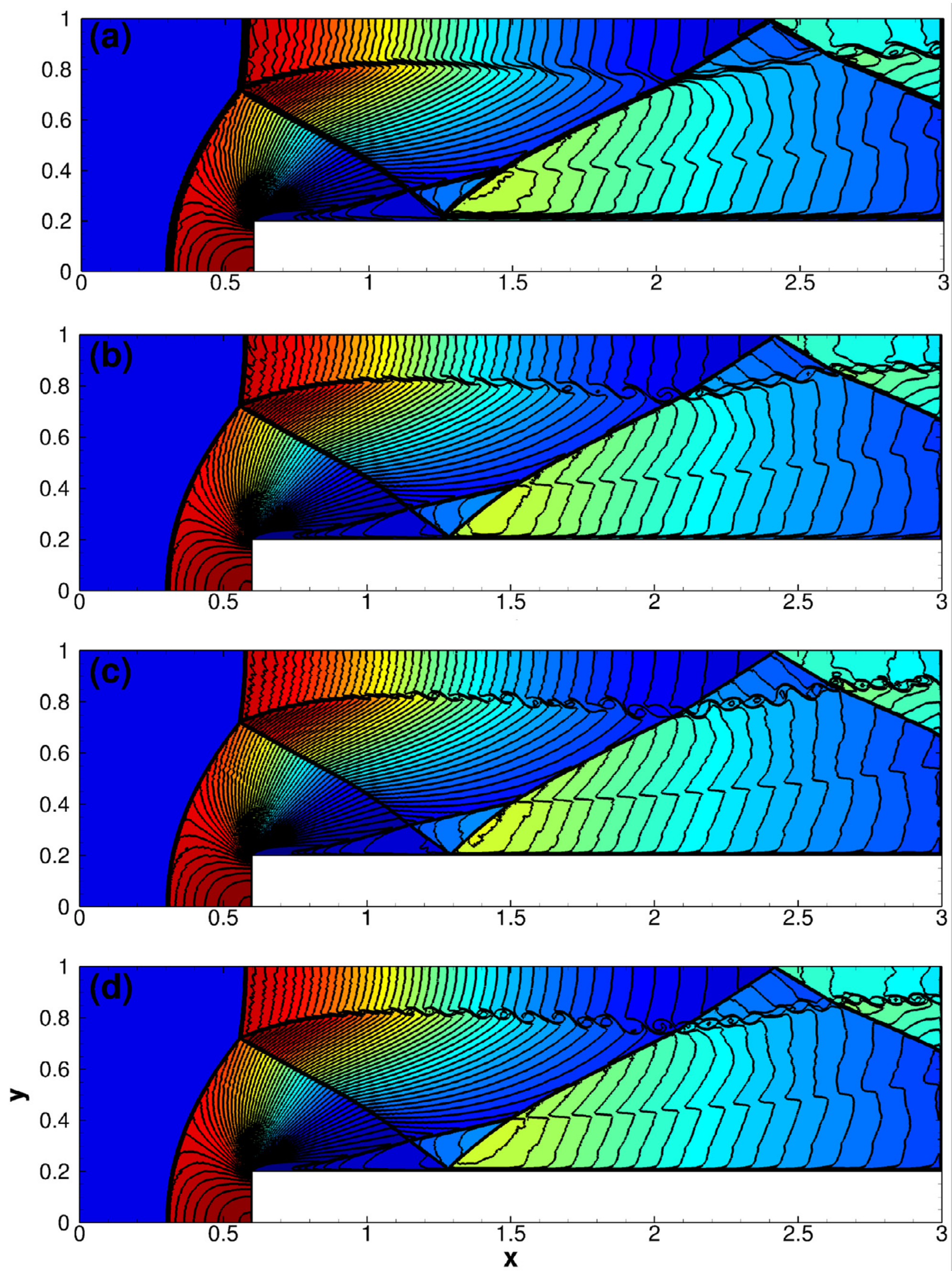

Fig. 10. Density contours for the Mach 3 wind tunnel flow with a forward step at $t = 4.0$ using $\Delta x = \Delta y = \frac{1}{240}$, CFL $= 0.6$. 50 equally spaced density contours from 0.32 to 6.15. From top to bottom: (a) WENO-JS5, (b) WENO-Z6, (c) WENO-CU6, (d) WENO-MSZ6.

and smooth regions. The square wave can be used to test the essentially non-oscillatory property of schemes. Fig. 4 show the numerical results at $t = 6$ computed with CFL $= 0.6$. We see that the resolution of all the schemes are comparable, even though the WENO-CU6 scheme shows slightly higher resolution due to the use of parameter $C = 20$ in the weights. Fig. 5 shows zones around $x = -0.2$ at $t = 6$ computed with $N = 3200$ grid cells and different CFL numbers. We can see that there are numerical oscillations for WENO-CU6 when CFL ≥ 0.7, for WENO-Z6 when CFL ≥ 0.8, and for WENO-MSZ6 when CFL ≥ 0.9. This shows that the present scheme tolerates larger CFL number thus has better stability compared with the WENO-CU6 and WENO-Z6 schemes.

4.2. 1D Euler systems

In this subsection, we present the numerical tests in the 1D Euler equations

$$\mathbf{U}_t + \mathbf{F}(\mathbf{U})_x = 0, \tag{35}$$

where

$$\mathbf{U} = (\rho, \rho u, E)^T, \quad \mathbf{F}(\mathbf{U}) = \left(\rho u, \rho u^2 + p, u(E+p)\right)^T.$$

The equation of state is given by

$$p = (\gamma - 1)\left(E - \frac{1}{2}\rho u^2\right),$$

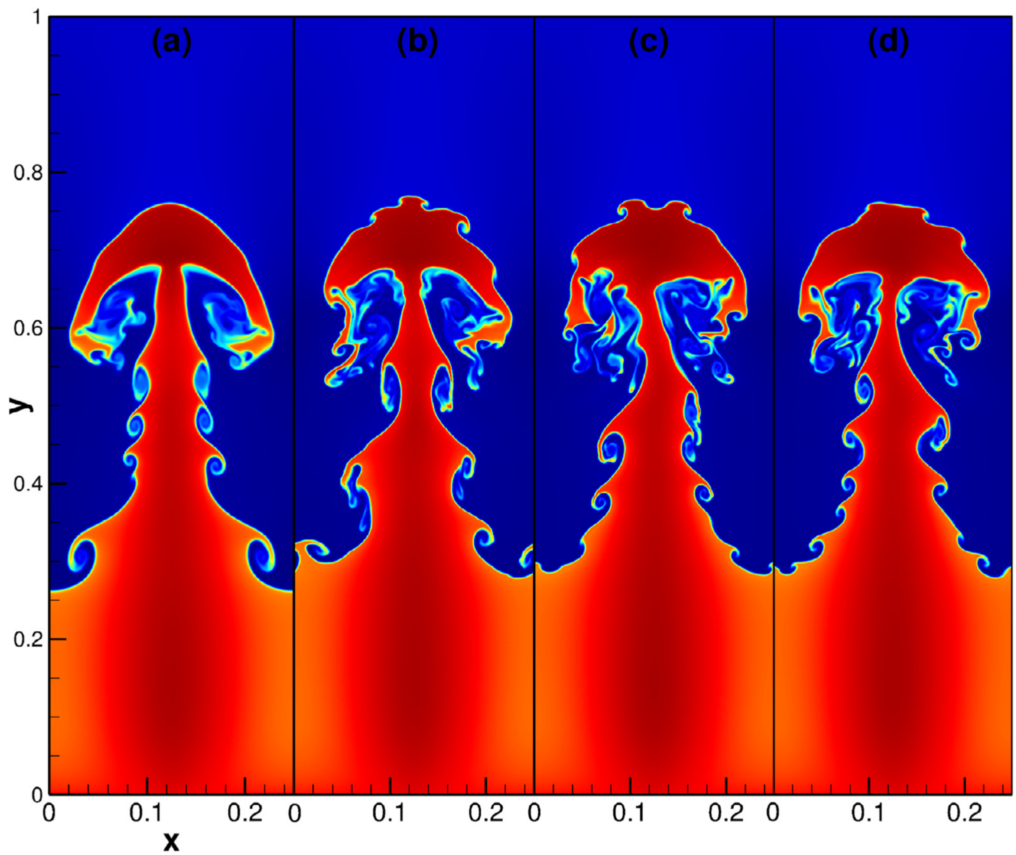

Fig. 11. Density contours of the Rayleigh-Taylor instability at $t = 1.95$ using $\Delta x = \Delta y = 1/240$, CFL= 0.6. From left to right: (a)WENO-JS5, (b) WENO-CU6 [21], (c) WENO-Z6 [20], (d) WENO-MSZ6.

where ρ, u, p and E are the density, velocity, pressure and total energy respectively, and γ is the ratio of specific heats and $\gamma = 1.4$ is used in all examples unless specified explicitly. The following four examples in 1D Euler systems are considered.

Example 1. (*Shock-entropy wave interaction*). We compute the shock-entropy wave interaction problem [23] on the interval $[-5, 5]$ with zero-gradient boundary conditions on both ends. The initial condition is given by

$$(\rho, u, p) = \begin{cases} (3.857143, 2.629369, 10.33333), & \text{if } -5 \le x < -4, \\ (1 + \lambda \sin(\kappa x), 0, 1), & \text{if } -4 \le x \le 5, \end{cases}$$

where $\lambda = 0.2$ and $\kappa = 5$ are the amplitude and wave number of the entropy wave, respectively. In this problem, a right-moving Mach 3 shock wave interacts with sine waves in a density disturbance that generates a flow field with both smooth structures and discontinuities. This flow induces wave trails behind a right-going shock at wave numbers higher than the initial density-variation wave number κ, which are progressing into smaller amplitude shocks. Since the exact solution is unknown, a reference solution is obtained by using the fifth-order WENO-JS scheme [5] with 3200 grid points. We compute the problem up to $t = 1.8$ with CFL $= 0.6$ on two grids with $\Delta x = 0.05$ and $\Delta x = 0.025$ respectively. Fig. 6 compares the computed density profiles with the reference solution. It is seen that the present WENO-MSZ6 captures shocks better than WENO-CU6 and WENO-Z6, especially in the high-frequency waves just behind the right going shock. By comparison, the WENO-MSZ6 scheme is the best.

Example 2. (*Shock tube problem*). For the Sod' shock tube problem [32], the initial condition is given by

$$(\rho, u, p) = \begin{cases} (1.000, 0, 1.0), & \text{if } 0 \le x < 0.5, \\ (0.125, 0, 0.1), & \text{if } 0.5 \le x \le 1.0. \end{cases} \tag{36}$$

We solve this problem up to $t = 0.2$ with $\Delta x = 0.005$. The CFL number is set to 0.6. The numerical density fields are displayed in Fig. 7. It is seen that the WENO-CU6 has produced overshoot at the contact discontinuity. The WENO-MSZ6 scheme shows slightly higher resolution of the contact discontinuity than the other two schemes, but it has a small overshoot at the shock. With CFL $= 0.8$ and $N = 400$ there will be overshoot for all the 6th-order WENO schemes near discontinuities, but the WENO-CU6 is most evident. So, it is suggested to use CFL number smaller than 0.6 for all the 6th-order WENO schemes.

Example 3. (*LeBlanc shock tube problem*). In this extreme shock tube problem [30,31], the computational domain is [0,9] filled with a perfect gas with $\gamma = 5/3$. The initial conditions are with high ratio of jumps for the internal energy and density. The jump for the internal energy is 10^6 and that for the density is 10^3. The initial conditions are given by

$$(\rho, u, e) = \begin{cases} (1.0, 0.0, 0.1), & \text{if } 0 \le x < 3, \\ (0.001, 0.000, 10^{-7}), & \text{if } 3 \le x \le 9. \end{cases}$$

We solve this problem up to $t = 6$ with $\Delta x = 9/400$ and $\Delta x = 9/800$ and CFL $= 0.6$. The computed velocity and internal energy fields are displayed in Fig. 8. We see that WENO-MSZ6 performs better than WENO-CU6 and WENO-Z6. An overshoot is produced, especially for the internal energy. However similar results were ob-

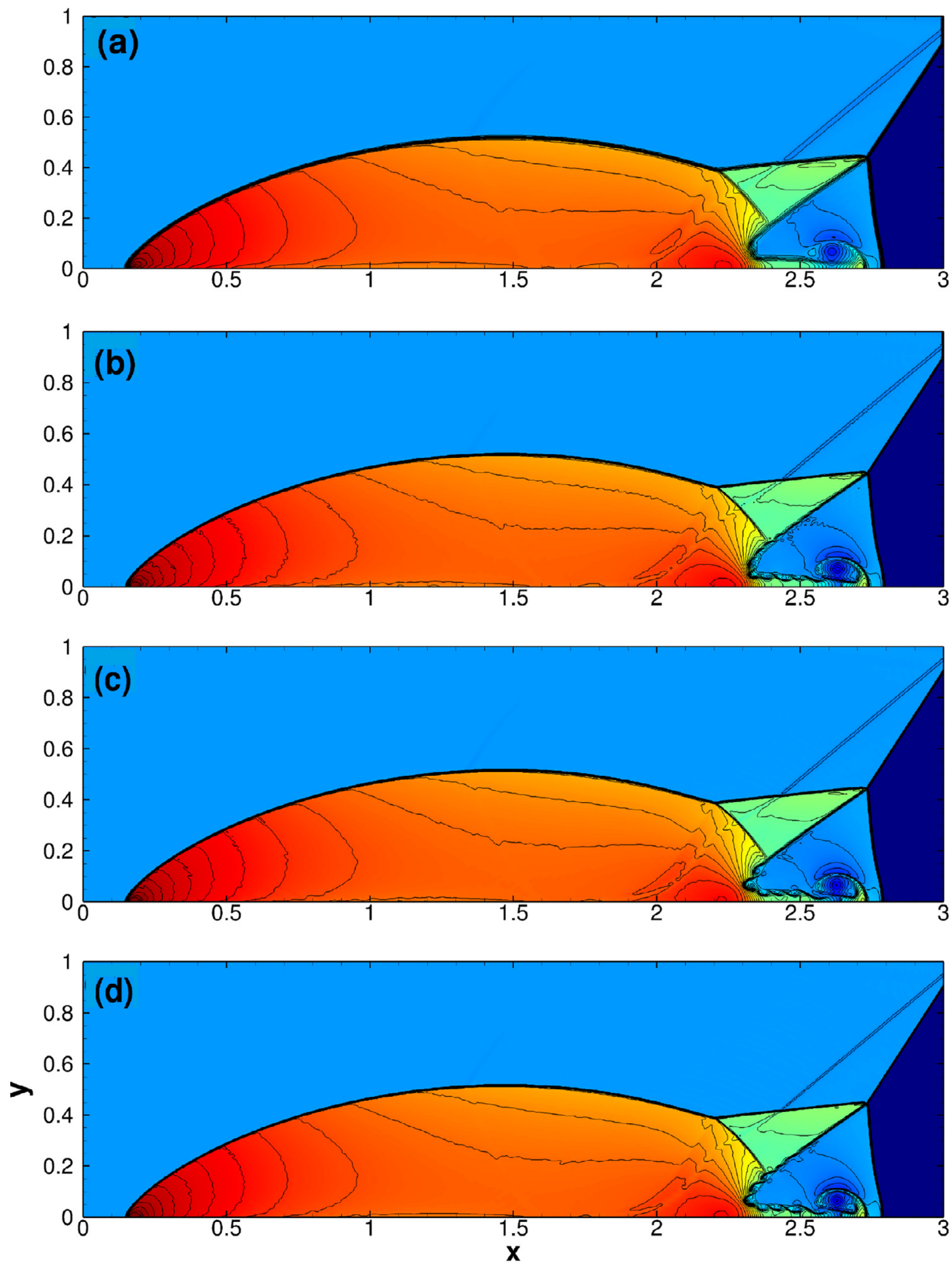

Fig. 12. Density contours of Double-Mach reflection of a Mach 10 shock wave with 30 contours lines from 1.8878 to 20.9144 at $t = 0.2$ using 800 × 200 grid cells and CFL = 0.6. (a) WENO-JS5, (b) WENO-CU6, (c) WENO-Z6, (d) WENO-MSZ6 schemes.

tained in [30,31]. Fig. 8 (bottom) shows that the numerical solution is greatly improved as the mesh is refined.

Example 4. (*Interacting blast waves*). The two-blast-wave interaction problem [1] is given by the initial condition

$$(\rho, u, p) = \begin{cases} (1, 0, 1000), & \text{if } \ 0 \le x < 0.1, \\ (1, 0, 0.01), & \text{if } 0.1 \le x < 0.9 \\ (1, 0, 100), & \text{if } 0.9 \le x \le 1. \end{cases}$$

The reflective boundary condition is applied at both $x = 0$ and $x = 1$. We solve this problem up to $t = 0.038$ with 400 grid points and CFL = 0.6. The reference solution is calculated by using the WENO-JS5 scheme [5] on 3200 grid points. Fig. 9 shows the computed density distributions. Again, all the schemes perform with high accuracy. The zoned region shows that the WENO-MSZ6 scheme produces slightly higher resolution than the WENO-CU6 and WENO-Z6 schemes around $x = 0.75$. Table 1 show the CPU time of three different schemes for computing the blast wave example. It is seen that the CPU time increases a little from WENO-Z6 to WENO-CU6 and WENO-MSZ6.

4.3. 2D Euler systems

In this subsection we apply the present WENO-MSZ6 scheme to solve the 2D compressible Euler systems of the form:

$$\mathbf{U}_t + \mathbf{F}(\mathbf{U})_x + \mathbf{G}(\mathbf{U})_y = 0, \tag{37}$$

where

$$\mathbf{U} = (\rho, \rho u, \rho v, E)^T,$$

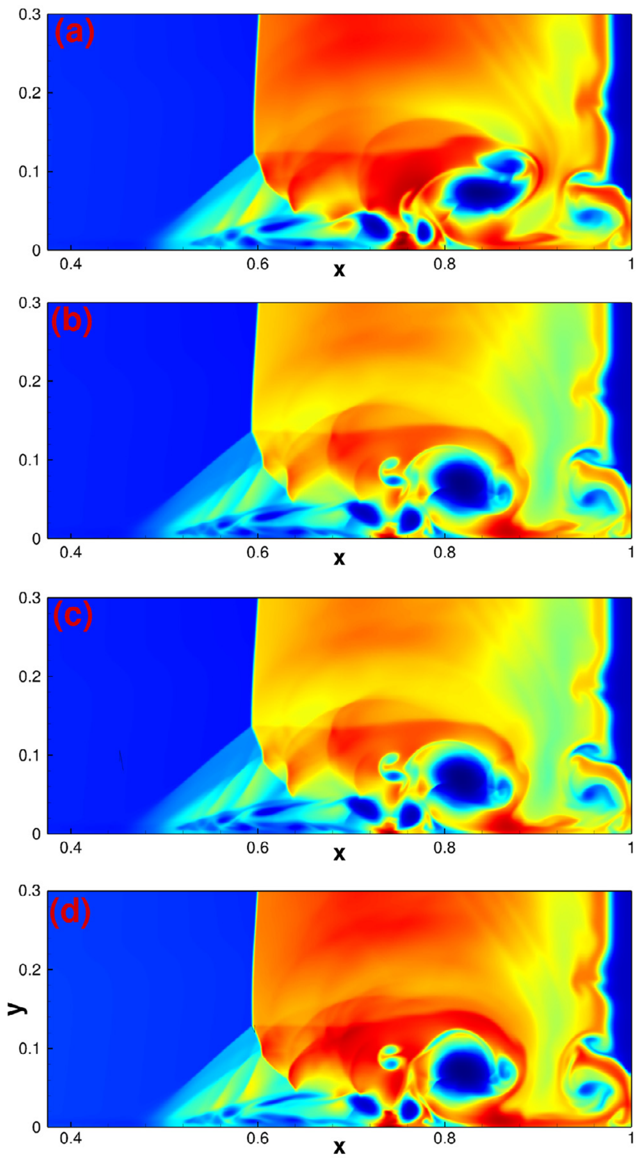

Fig. 13. Density contours of viscous shock tube using 1000 × 500 grid points and CFL = 0.6, $Re = 1000$, $t = 1$. (a) WENO-JS5, (b) WENO-CU6, (c) WENO-Z6, (d) WENO-MSZ6.

$$\mathbf{F}(\mathbf{U}) = (\rho u, \rho u^2 + p, \rho uv, u(E+p))^T,$$
$$\mathbf{G}(\mathbf{U}) = (\rho v, \rho vu, \rho v^2 + p, v(E+p))^T,$$
$$p = (\gamma - 1)\left(E - \frac{1}{2}\rho(u^2 + v^2)\right). \tag{38}$$

Here ρ, u, v, p and E are density, components of velocity in the x and y coordinate directions, pressure and total energy, respectively. The following three examples in 2D Euler systems are considered.

Example 1 (*Mach 3 wind tunnel flow with a step*). Mach 3 wind tunnel flow with a forward step [1] is widely used to verify the capability of high-resolution schemes [17,33] in capturing shock-rich flow structures generated from boundary reflections. In this problem, a uniform Mach 3 flow is flown into a wind tunnel of [0, 3] × [0, 1] with a step of 0.2 units high located at 0.6 units away from the left end of the tunnel. Supersonic inflow and outflow conditions are imposed on the left and right ends while a reflective condition is imposed on the remaining boundaries. We compare the numerical results at $t = 4.0$ in Fig. 10. It is seen that the shock waves and discontinuities are captured well. An examination of these results reveals that WENO-MSZ6 predicts the formation of vortices on the slip line earlier than the WENO-Z6 and WENO-CU6 schemes, and the three schemes have higher resolution compared with the fifth-order WENO-JS5 scheme.

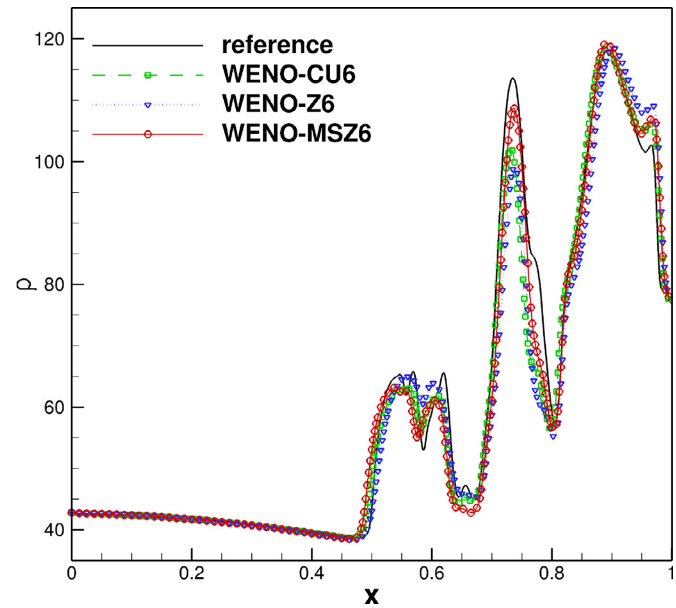

Fig. 14. Distribution of the density along the bottom wall of the tube at $t = 1$ for $Re = 1000$. The reference solution is computed by using WENO-JS5 on the 2500 × 1250 grid.

Example 2 (*Rayleigh-Taylor instability*). Rayleigh-Taylor instability happens on an interface between two fluids of different densities when an acceleration is directed from heavier fluid to lighter fluid. This problem has been simulated extensively in the literature (e.g., [16,34,35]). The computational domain is [0, 1/4] × [0, 1] and the initial conditions are

$$(\rho, u, v, p) = \begin{cases} (2, 0, -0.025a\cos(8\pi x), 2y+1), & \text{if } 0 \le y < 0.5, \\ (1, 0, -0.025a\cos(8\pi x), y+1.5), & \text{if } 0.5 \le y < 1, \end{cases}$$

with the ratio of specific heats $\gamma = 5/3$. The gravitational effect is introduced by adding the source term $S = (0, 0, \rho, \rho v)^T$ to the right-hand side of the 2D Euler Eq. (37). Reflective boundary conditions are imposed for the left and right boundaries, and the top and bottom boundaries are set as $(\rho, u, v, p) = (1, 0, 0, 2.5)$ and $(\rho, u, v, p) = (2, 0, 0, 1)$, respectively. The CFL number is set to 0.6. The final simulation time is $t = 1.95$. The density contours plotted in Fig. 11 show that the WENO-MSZ6 scheme obtains richer structures than the WENO-CU6 and WENO-Z6 schemes, particularly, it produces more vortices on the interface, indicating that it is less dissipative than the other schemes.

Example 3 (*Double Mach reflection of a strong shock*). We consider the two dimensional double Mach reflection problem of a shock off an oblique surface which describes the reflection of a planar Mach shock in air hitting a wedge [1]. We calculate this problem on [0, 4] × [0, 1] domain and display the results in [0, 3] × [0, 1] as customary. Initially a right-moving Mach 10 shock is imposed and the shock front makes an angle of 60° with the x axis at $x = 1/6$. The region from $x = 0$ to $x = 1/6$ along the bottom boundary is assigned the exact values of the initial post-shock flow and a reflecting boundary condition is taken for the rest. The left end boundary is assigned the values of the initial post-shock flow. For the right end boundary at $x = 4$, all gradi-

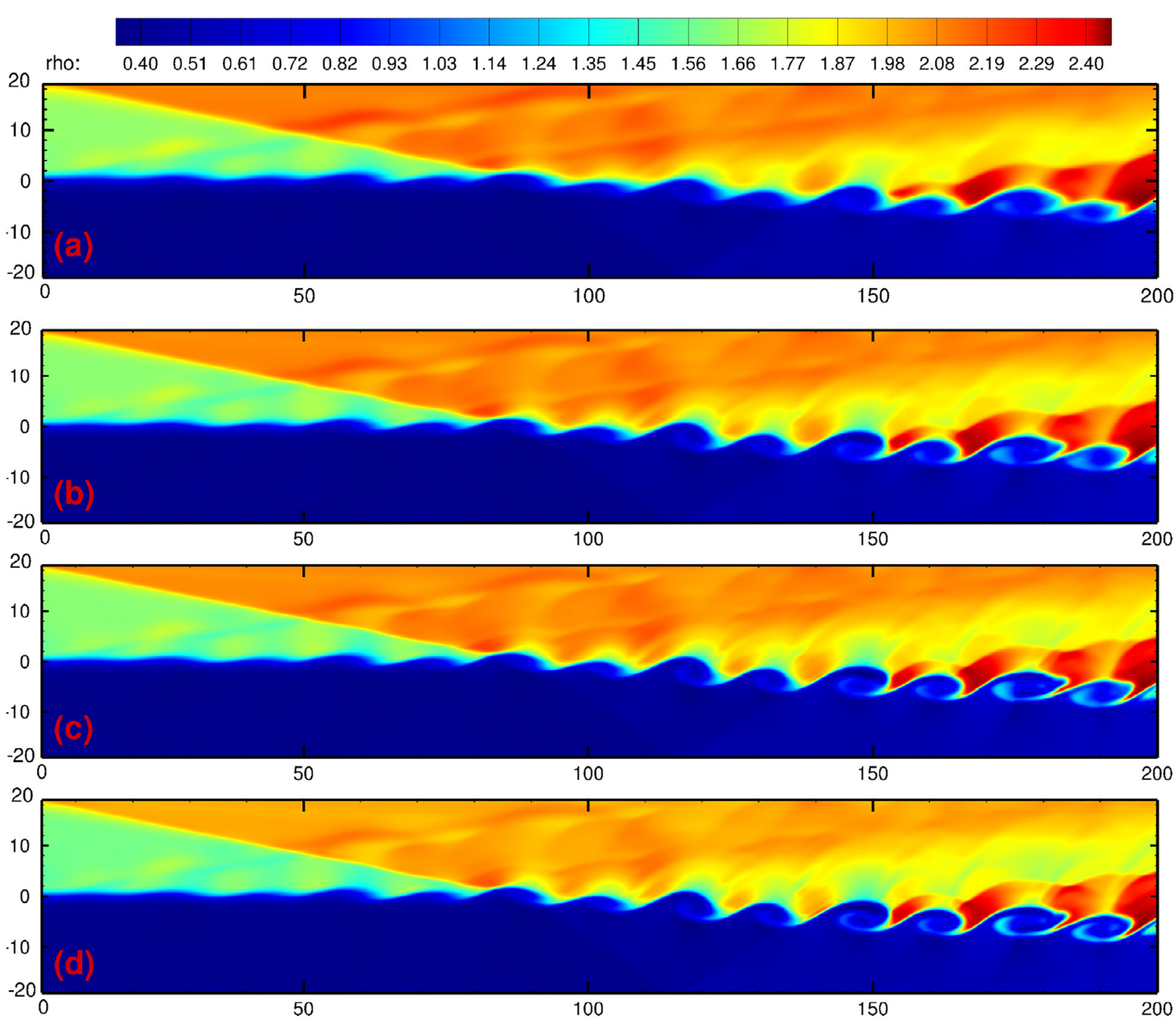

Fig. 15. Density contours of shock/mixing layer interaction, CFL = 0.6, $Re = 500$, $t = 120$, 320×80 grid points. From (a) to (d): WENO-JS5, WENO-CU6, WENO-Z6, WENO-MSZ6.

ents are set to zero. The top boundary is set to describe the exact motion of the Mach 10 shock. See [1] and [22] for a detailed description of the computational setup. We solve the problem up to time $t = 0.2$ using $\Delta x = \Delta y = 1/200$. The numerical results of density contours obtained using the WENO-JS5, WENO-CU6, WENO-Z6 and WENO-MSZ6 schemes are displayed in Fig. 12. We see that the WENO-MSZ6 and WENO-CU6 schemes resolve the instabilities around the Mach stem better than the WENO-Z6 scheme, and the three schemes are better than the WENO-JS5 scheme.

4.4. 2D viscous shock tube problem

From this subsection onward we evaluate the capability of the present scheme in resolving viscous flows. In this subsection we consider the 2D viscous shock tube problem in a square tube with unit side length and insulated walls. This problem has been simulated in many papers [36–39]. The governing equations are the 2D compressible Navier-Stokes equations

$$\mathbf{U}_t + \mathbf{F}(\mathbf{U})_x + \mathbf{G}(\mathbf{U})_y = \mathbf{F}^v(\mathbf{U})_x + \mathbf{G}^v(\mathbf{U})_y, \tag{39}$$

where the conservative variables $\mathbf{U}$ and inviscid fluxes $\mathbf{F}$ and $\mathbf{G}$ are given in (38), and the viscous fluxes $\mathbf{F}^v$ and $\mathbf{G}^v$ are given by [37]

$$\mathbf{F}^v(\mathbf{U}) = \left[0,\ \tau_{xx} = \lambda(u_x + v_y) + 2\mu u_x,\ \tau_{xy} = \mu(u_y + v_x),\ u\tau_{xx} + v\tau_{xy} + \frac{\gamma\mu}{Pr} e_x\right]^T,$$

$$\mathbf{G}^v(\mathbf{U}) = \left[0,\ \tau_{yx} = \tau_{xy},\ \tau_{yy} = \lambda(u_x + v_y) + 2\mu v_y,\ u\tau_{yx} + v\tau_{yy} + \frac{\gamma\mu}{Pr} e_y\right]^T.$$

As usual, the pressure p is given by the perfect gas law $p = (\gamma - 1)\rho e$, where e is the specific internal energy. The fluid is assumed as ideal gas with $\gamma = 1.4$, constant viscosity coefficients $\mu = 1/Re$, $\lambda = -2\mu/3$ are assumed for this problem as [37], where Re is the Reynolds number, and the Prandtl number $Pr = 0.73$. The initial states on the left and right regions of the diaphragm located vertically at the middle of the tube are $(\rho, u, v, p)_L = (120, 0, 0, 120/\gamma), 0 \le x \le 0.5$, and $(\rho, u, v, p)_R = (1.2, 0, 0, 1.2/\gamma), 0.5 < x \le 1$. The diaphragm is broken at $t = 0$. A shock wave forms, followed by a contact discontinuity, and travels to the right. In the same time, a rarefaction wave expands in both directions. The incident shock wave induces a boundary layer along the horizontal wall. The shock reflects at the

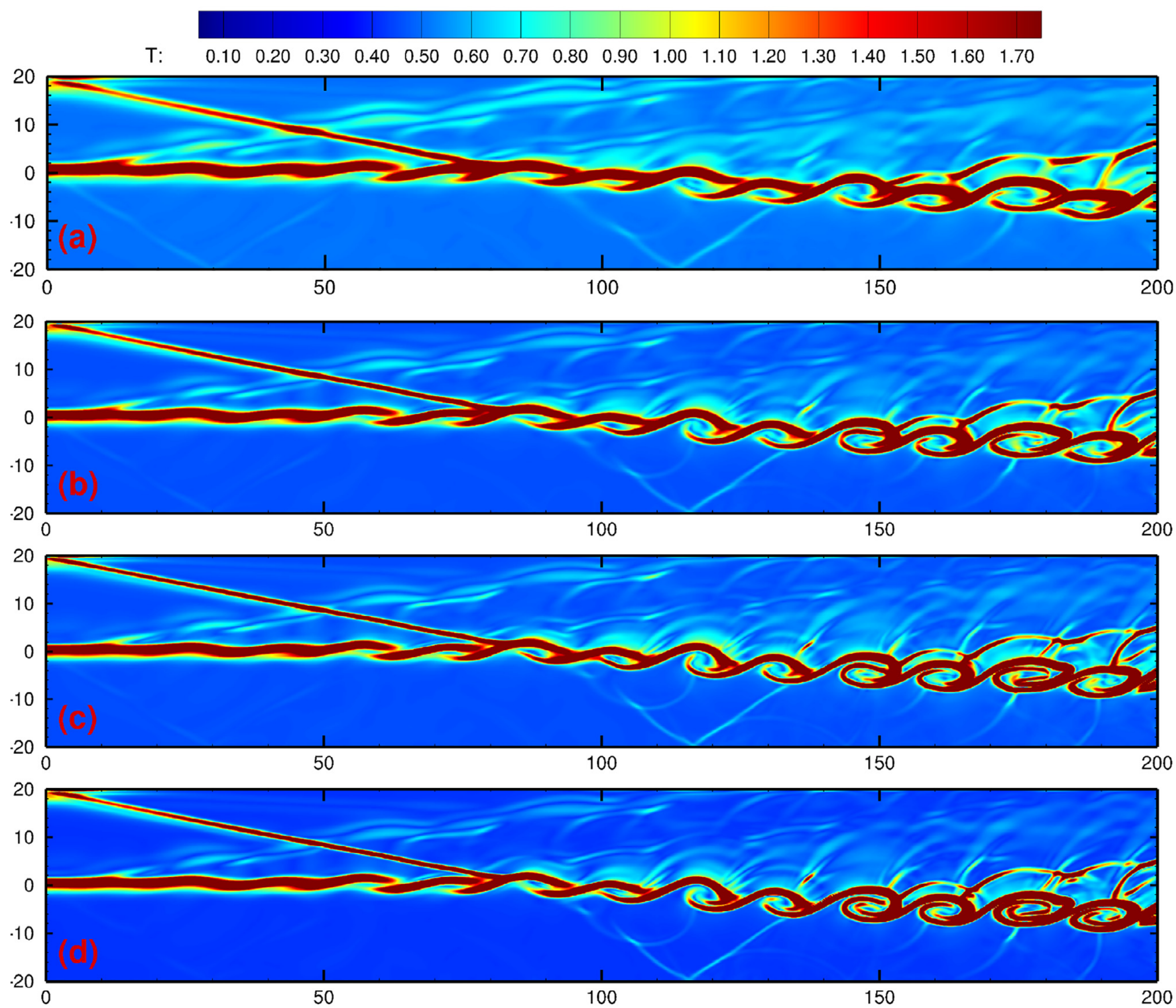

Fig. 16. Numerical schlieren according to $T = 0.95 \times \exp(-2.0|\nabla\rho|)$ of shock/mixing layer interaction, CFL = 0.6, $Re = 500$, $t = 120$, 320×80 grid points. From (a) to (d): WENO-JS5, WENO-CU6, WENO-Z6, WENO-MSZ6.

right wall at $t \approx 0.21$, and interacts with the contact discontinuity and the boundary layer, creating a complex flow field typical of separation bubbles, a typical "λ-shape" shock pattern in the boundary layer, a slip line, and rolled-up vortices. By applying the symmetry condition at the upper boundary, the computational domain is $[0,\ 1] \times [0,\ 0.5]$. For the left, bottom and right boundaries, non-slip and adiabatic wall conditions are applied.

The viscous and heat diffusion terms are calculated by a 6th-order central scheme [40]. The Reynolds number is $Re = 1000$. The computations have been performed using four different schemes: WENO-JS, WENO-CU6, WENO-Z6 and WENO-MSZ6, on 1000×500 points. Fig. 13 shows a comparison of the density contours at $t = 1$. At this time the shock has reflected from the right end wall and goes into the zone of the rarefaction wave [37,38]. The contact discontinuity has interacted with the reflected shock and stays almost stationary, close to the right wall. The results of different schemes are similar, however, differences can be observed near the bottom wall, especially, the 6th-order WENO-CU6, WENO-Z6 and WENO-MSZ6 schemes resolve the slip line emanating from the triple point of the "λ-shape" shock pattern better than the 5th-order WENO-JS scheme. Fig. 14 shows a comparison of the density distributions along the bottom wall among various WENO schemes. It is seen that the result of WENO-MSZ6 has a highest peak at $x \approx 0.88$, in agrement with the trend in [37–39].

4.5. Shock/mixing layer interaction

The problem of a shock wave impingement on a mixing layer is used to assess the performance of numerical schemes [41–43]. In the problem, a spatially developing mixing layer has an initial convective Mach number $M_c = (u_1 - u_2)/(c_1 + c_2) = 0.6$, and an oblique shock with a wedge angle of $\beta = 12^\circ$ and incident from the upper-left corner interacts with the vortices generated from the instability of the shear layer. The incident oblique shock is refracted by the shear layer and then reflects from the bottom slip wall, and transmits the shear layer again. At the same time, alternate compression-expansion fans form around the shear layer. Downstream the transmitting position, a series of shocklets (small transient shocks) form around the vortices. The outflow boundary has been arranged to be supersonic everywhere. The computational domain is $[0, 200] \times [-20, 20]$. At $x = 0$, the supersonic inflow boundary condition has a hyperbolic tangent velocity profile,

$$u = \frac{1}{2}[(u_1 + u_2) + \tanh(2y)], \quad v = 0.$$

For the upper stream of the shear layer $(y \geq 0), u_1 = 3, \rho_1 = 1.6374, p_1 = 0.3327$ and for the lower stream $(y < 0), u_2 = 2, \rho_2 = 0.3626, p_2 = 0.3327$. The post shock states of the incident oblique shock are set at the upper boundary, and slip-adiabatic wall conditions are assumed at the bottom boundary to avoid any boundary-layer formation and subsequent complexities. Transverse-velocity fluctuations are added to the y velocity component at the inlet:

$$v' = \sum_{k=1}^{2} a_k \cos(2\pi kt/T + \phi_k) \exp(-y^2/b),$$

where $b = 10,\ a_1 = a_2 = 0.05,\ \phi_1 = 0,\ \phi_2 = \pi/2,\ T = \lambda/u_c$ is the period, $\lambda = 30$ is the wavelength, $u_c = 2.68$ is the convective velocity [41]. The Prandtl number *Pr* is set to 0.72 and the Reynolds number *Re* is chosen to be 500, and the ratio of specific heats $\gamma = 1.4$. The dynamic viscosity μ is calculated according to the Sutherland law for this example. Figs. 15 and 16 show the numerical density contours and schlieren based on density respectively computed with the 320×80 grid. We see that the results of the four schemes are similar, and the schlieren graphs in Fig. 16 show more clearly the refracted and transmitted shocks, shocklets downstream the transmission, vortices, and expansion fans. We can also see that the three 6th-order WENO schemes have almost the same resolution, which is higher than the WENO-JS5 scheme.

5. Conclusions

A new central-upwind 6th-order WENO scheme (WENO-MSZ6) based on modified candidate stencil approximations is presented. The four stencil approximations achieve 4th-order accuracy thus the sufficient condition for the optimal 6th-order accuracy can be one order lower than that in previous 6th-order WENO schemes. A reference smoothness indicator is used to achieve the optimal order even at critical points. We compare the present scheme with the two recently developed WENO-CU6 and WENO-Z6 schemes. A number of 1D and 2D numerical examples show that the present scheme produces higher resolution and can tolerate a larger CFL number for the occurrence of visible oscillations near discontinuities compared with other two 6th-order WENO schemes. However, the robustness of the present WENO-MSZ6 scheme for calculating strong discontinuities has not been tested fully. It needs to be tested in more numerical problems.

Declaration of Competing Interest

We declare that we have no financial and personal relationships with other people or organizations that can inappropriately influence our work, there is no professional or other personal interest of any nature or kind in any product, service and/or company that could be construed as influencing the position presented in, or the review of, the manuscript entitled.

CRediT authorship contribution statement

Yahui Wang: Methodology, Software, Writing - original draft. **Yulong Du:** Methodology, Visualization. **Kunlei Zhao:** Methodology, Visualization. **Li Yuan:** Supervision, Methodology, Writing - review & editing.

Acknowledgements

This work is supported by Natural Science Foundation of China (91641107, 91852116), Fundamental Research of Civil Aircraft (MJ-F-2012-04).

References

[1] Woodward P, Collela P. The numerical simulation of two dimensional fluid flow with strong shocks. J Comput Phys 1984;54:115–73.
[2] Harten A, Osher S. Uniformly high order essentially non-oscillatory schemes I. SIAM J Numer Anal 1987;24:279–309.
[3] Harten A, Engquist B, Osher S, Chakravarthy S. Uniformly high order essentially non-oscillatory schemes III. J Comput Phys 1987;71:231–303.
[4] Liu XD, Osher S, Chan T. Weighted essentially non-oscillatory schemes. J Comput Phys 1994;115:200–12.
[5] Jiang GS, Shu CW. Efficient implementation of weighted ENO schemes. J Comput Phys 1996;126:202–28.
[6] Cockburn B, Shu CW. TVB Runge-Kutta local projection discontinuous Galerkin finite element method for conservation laws II: general framework. Math Comp 1989;52:411–35.
[7] Bassi F, Rebay S. High-order accurate discontinuous finite element solution of the 2D Euler equations. J Comput Phys 1997;138:251–85.
[8] Suresh A, Huynh HT. Accurate monotonicity-preserving schemes with Runge-Kutta time stepping. J Comput Phys 1997;136:83–99.
[9] Adams NA, Shariff K. A high-resolution hybrid compact-ENO scheme for shock--turbulence interaction problems. J Comput Phys 1996;127:27–51.
[10] Pirozzoli S. Conservative hybrid compact-WENO schemes for shock-turbulence interaction. J Comput Phys 2002;178:81–117.
[11] Ren YX, Liu M, Zhang H. A characteristic-wise hybrid compact-weno scheme for solving hyperbolic conservation laws. J Comput Phys 2003;192:365–86.
[12] Henrick AK, Aslam TD, Powers JM. Mapped weighted essentially non-oscillatory schemes: achieving optimal order near critical points. J Comput Phys 2005;207:542–67.
[13] Borges R, Carmona M, Costa B, Don WS. An improved weighted essentially non-oscillation scheme for hypebolic conservation laws. J Comput Phys 2008;227:3191–211.
[14] Castro M, Costa B, Don WS. High order weighted essentially non-oscillatory WENO-Z schemes for hyperbolic conservation laws. J Comput Phys 2011;230:1766–92.
[15] Chang HK, Ha Y, Yoon J. Modified non-linear weights for fifth-order weighted essentially non-oscillatory schemes. J Sci Comput 2016;67:299–323.
[16] Zeng FJ, Shen YQ, Liu SP. A perturbational weighted essentially non-oscillatory scheme. Comput Fluids 2018;172:196–208.
[17] Zhu J, Qiu JX. A new fifth order finite difference WENO scheme for solving hyperbolic conservation laws. J Comput Phys 2016;318:110–21.
[18] Wang YH, Du YL, Zhao KL, Yuan L. Modified stencil approximations for fifth-order weighted essentially non-oscillatory schemes. J Sci Comput 2019;81:898–922.
[19] Martin MP, Taylor EM, Wu M, Weirs VG. A bandwidth-optimized weno scheme for the effective direct numerical simulation of compressible turbulence. J Comput Phys 2006;220:270–89.
[20] Yamaleev NK, Carpenter MH. A systematic methodology for constructing high--order energy stable WENO schemes. J Comput Phys 2009;228:4248–72.
[21] Hu XY, Wang Q, Adams NA. An adaptive central-upwind weighted essentially non-oscillatory scheme. J Comput Phys 2010;229:8952–65.
[22] Hu FX. The 6th-order weighted ENO schemes for hyperbolic conservation laws. Comput Fluids 2018;174:34–45.
[23] Feng H, Hu F, Wang R. A new mapped weighted essentially non-oscillatory scheme. J Sci Comput 2012;51:449–73.
[24] Wang R, Feng H, Huang C. A new mapped weighted essentially non-oscillatory method using rational mapping function. J Sci Comput 2015;67:540–80.
[25] Shu CW, Osher S. Efficient implementation of essentially non-oscillatory shock--capturing schemes II. J Comput Phys 1989;83:32–78.
[26] Shu CW. Essentially non-oscillatory and weighted essentially non-oscillatory schemes for hyperbolic conservation laws. in: advanced numerical approximation of nonlinear hyperbolic equations. in: lecture notes in mathematics, 1697. Berlin, Springer-Verlag; 1998. p. 325–432.
[27] Taylor EM, Wu M, Martin MP. Optimization of nonlinear error for weighted essentially non-oscillatory methods in direct numerical simulations of compressible turbulence. J Comput Phys 2007;223:384–97.
[28] Shu CW. Total-variation-diminishing time discretizations. SIAM J Sci Statist Comput 1988;9(6):1073–84.
[29] Gottlieb S, Shu CW. Total variation diminishing Runge-Kutta schemes. Math Comp 1998;67:73–85.
[30] Liu W, Cheng J, Shu CW. High order conservative Lagrangian schemes with Lax-wendroff type time discretization for the compressible Euler equations. J Comput Phys 2009;228:8872–91.
[31] Loubre R, Shashkov MJ. A subcell remapping method on staggered polygonal grids for Arbitrary-Lagrangian-Eulerian methods. J Comput Phys 2005;209:105–38.
[32] Sod GA. A survey of several finite difference methods for systems of nonlinear hyperbolic conservation laws. J Comput Phys 1978;107:1–31.

[33] Liu HX. A numerical study of the performance of alternative weighted ENO methods based on various numerical fluxes for conservation law. Appl Math Comput 2017;296:182–97.
[34] Glimm J, Grove J, Li X, Oh W, Tan DC. The dynamics of bubble growth for Rayleigh-Taylor unstable interfaces. Phys Fluids 1988;31:447–65.
[35] Young YN, Tufo H, Dubey A, Rosner R. On the miscible Rayleigh-Taylor instability: two and three dimensions. J Fluid Mech 2001;447:377–408.
[36] Arora M, Roe PL. A well-behaved TVD limiter for high-resolution calculations of unsteady flows. J Comput Phys 1997;132:3–11.
[37] Daru V, Tenaud C. Evaluation of TVD high resolution schemes for unsteady viscous shocked flows. Comput Fluids 2001;30:89–113.
[38] Zhou GZ, Xu K, Liu F. Grid-converged solution and analysis of the unsteady viscous flow in a two-dimensional shock tube. Phys Fluids 2018;30(1):016102.
[39] Sun ZS, Ren YX, Zha BL, Zhang SY. High order boundary conditions for high order finite difference schemes on curvilinear coordinates solving compressible flows. J Sci Comput 2015;65:790–820.
[40] Hirsh RS. Higher order accurate difference solutions of fluid mechanics problems by a compact differencing technique. J Comput Phys 1975;19:90–109.
[41] Yee HC, Sandham ND, Djomehri MJ. Low-dissipative high-order shock capturing methods using characteristic-based filters. J Comput Phys 1999;150(1):199–238.
[42] Chaudhuir A, Hadjadj A, Chinnayya A, Palerm S. Numerical study of compressible mixing layers using high-order WENO schemes. J Sci Comput 2011;47:170–97.
[43] Liu XL, Zhang SH. Direct numerical simulation of the interaction of 2D shock wave and shear layer. Chin J Theor Appl Mech 2013;45:61–75 (in Chinese).